Open Access

This article is licensed under CC-BY-NC-ND 4.0

Article

Cyclohexylalanine-Containing α-Helical Amphipathic Peptide Targets Cardiolipin, Rescuing Mitochondrial Dysfunction in Kidney Injury

Gwangsu Shin, Soonsil Hyun, Dongwoo Kim, Yoonhwa Choi, Kyu Hong Kim, Dongmin Kim, Soie Kwon, Yon Su Kim,* Seung Hee Yang,* and Jaehoon Yu*

Cite This: J. Med. Chem. 2024, 67, 3385−3399

Read Online

ACCESS | Metrics & More | Article Recommendations | Supporting Information

ABSTRACT: Mitochondrial dysfunction is linked to degenerative diseases, resulting from cardiolipin (CL)-induced disruption of cristae structure in the inner mitochondrial membrane (IMM); therefore, preserving cristae and preventing CL remodeling offer effective strategies to maintain mitochondrial function. To identify reactive oxygen species (ROS)-blocking agents against mitochondrial dysfunction, a library of cyclohexylamine-containing cell-penetrating α-helical amphipathic "bundle" peptides were screened. Among these, CMP3013 is selectively bound to abnormal mitochondria, preserving the cristae structure impaired by mitochondria-damaging agents. With a stronger affinity for CL compared with other IMM lipid components, CMP3013 exhibited high selectivity. Consequently, it protected cristae, reduced ROS production, and enhanced adenosine triphosphate (ATP) generation. In mouse models of acute kidney injury, a 1 mg/kg dose of CMP3013 demonstrated remarkable efficacy, highlighting its potential as a therapeutic agent for mitochondrial dysfunction-related disorders. Overall, CMP3013 represents a promising agent for mitigating mitochondrial dysfunction and associated diseases.
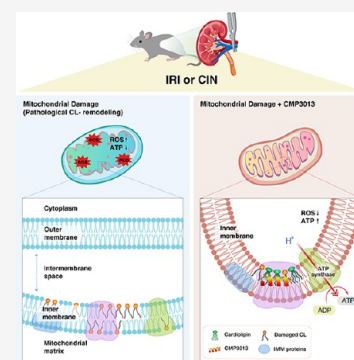
1. INTRODUCTION

Mitochondria are vital organelles, producing essential adenosine triphosphate (ATP) for cell survival. Mitochondrial dysfunction, caused by DNA damage or environmental stresses, leads to intrinsic mitochondrial diseases[1] and degenerative diseases.[2,3] Cardiolipin (CL) is an essential phospholipid for the unique cristae structure of the mitochondrial inner membrane.[4] Accumulating evidence suggests that mitochondrial dysfunction can result from the destruction of cristae structure due to CL remodeling.[5−7] CL, located exclusively in the inner membrane of mitochondria (IMM), is composed of two phosphate and four fatty acid moieties and plays a crucial role in maintaining proper protein complex function by inducing negative curvature and ensuring membrane structure stability.[8] Pathological CL remodeling, induced by peroxidation and CL content reduction, leads to membrane leakage and a loss of function of IMM protein complexes. Identifying the key regulators that maintain cristae structure[9] is a challenging task in the context of preventing pathological CL remodeling. Nevertheless, finding molecules that specifically bind to CL offers a promising approach to prevent oxidation and preserve mitochondrial function.

Typical lipophilic cations containing a triphenylphosphonium moiety may serve as CL binding agents; however, their one positive charge leads to nonspecific binding to any membrane phospholipid. The Szeto−Schiller (SS) peptide,[10] a mitochondria-specific agent, interacts weakly with CL despite its alternating hydrophilic and hydrophobic amino acids (aa). The positively charged ammonium and aromatic moieties in this β-sheet peptide interact with the phosphate and fatty acid components of CL, respectively; however, the affinity of the SS peptide against CL is relatively weak (low micromolar).[11] Expanding the β-sheet peptide sequence beyond 6 aa enhances mitochondrial penetration and specificity but also leads to severe toxicity at micromolar levels.[12] In a previous study,[13] we discovered new factors governing the cell penetration abilities of α-helical dimeric bundles. First, we demonstrated that 10-aa long monomer peptides in this family rapidly form oxidative dimeric bundles. Second, we found that substitution(s) of hydrophobic or hydrophilic residue(s) for Leu and Lys in the original monomer peptides did not alter oxidative dimeric bundle formation or cell penetration ability.[14] We identified a cell-penetrating bundle dimer peptide based on the LR10 monomer, which rapidly forms oxidative dimeric bundles and readily enters cells at nanomolar concentrations. This peptide may target mitochondria or CL owing to its four positively
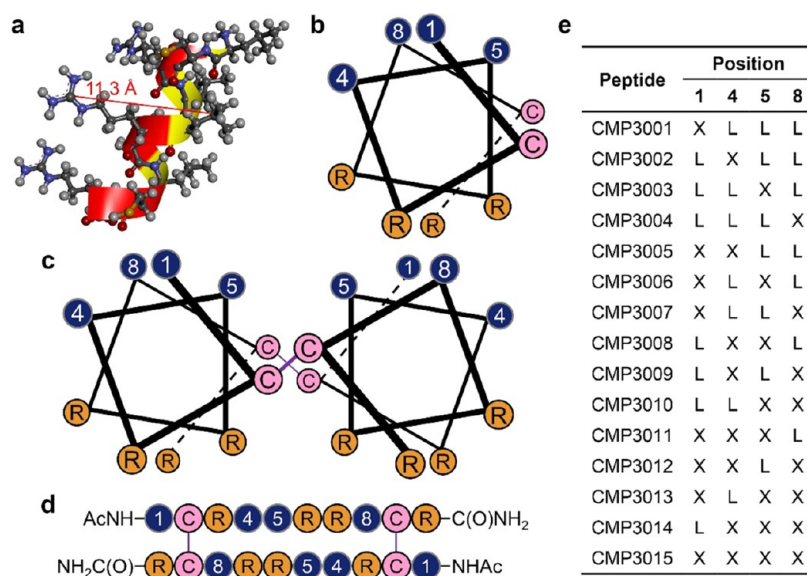
Figure 1. Schematic structures of 10-aa long monomeric and dimeric α-helical peptides. (a) Model of the typical α-helix peptide drawn using Biovia Discovery Studio 2020 (Dassault Systems, Massachusetts). A distance monitor was used to calculate the distance between two carbon atoms on the side chain at the fifth position Leu and seventh position Arg. Monomers in the peptide library are based on the following sequence: AcNH-LCRLLRRLCR-C(O)NH$_2$. (b, c) Wheel diagrams of the monomeric α-helical peptide and the dimeric bundle peptide, respectively. The monomer peptide was air-oxidized to generate the dimeric bundle by two disulfide bonds (purple line). Dark blue circles represent hydrophobic residues (Leu or Cha); orange circles are hydrophilic Arg, C: Cys. (d) Simplified antiparallel structure of the dimeric bundle peptide. The position of the hydrophobic amino acid is designated as 1, 4, 5, or 8. Refer to Figure S3 for details. (e) Hydrophobic amino acids for each peptide in the library. The position 1, 4, 5, or 8 is identical to that in Figure 1b−d. X: Cha.

charged residues, capable of strong binding to multiple CLs, and its hydrophobic moieties that interact with the fatty acidic region of CL. Introducing highly hydrophobic aa residues, such as cyclohexylalanine (Cha), into a peptide library enhances selective recognition and strong interactions with CLs in the IMM.[15] These bundled dimers are expected to penetrate cells at low nanomolar concentrations, minimizing the cytotoxicity associated with nonselective binding to monophosphoric lipids.

Ischemic acute kidney injury (AKI), characterized by a sudden loss of renal function,[16−18] is a short-term complication affecting native kidneys and renal allografts. Antibiotic overuse, particularly in patients with multiple drug resistance, may contribute to undesirable kidney side effects, such as colistin-induced nephrotoxicity (CIN),[19] with colistin being a polymyxin antibiotic used to treat Gram-negative bacterial infections. During the COVID-19 pandemic, clinical attention on nephrotoxic AKI markedly increased.[20] Although oxidative stress and mitochondrial dysfunction are promising targets for CIN treatment, the molecular mechanisms underlying CIN in renal mitochondria remain unknown.[21,22]

In this study, we used CMP3013, a protective agent targeting nephrotoxic AKI and colistin-induced mitochondrial dysfunction. CMP3013, derived from our peptide library, preferentially binds to aberrant and damaged mitochondria, preserving the cristae structure and protecting against damage caused by harmful agents. Its four positively charged moieties enable tight binding to CL molecules, compared with other lipid components in the IMM. *In vitro* cell and *in vivo* animal studies demonstrated that CMP3013 preserved the cristae structure, resulting in enhanced ATP production, increased mitochondrial membrane potential, promotion of normal mitochondrial function, and improved kidney function during nephrotoxic AKI.

2. RESULTS AND DISCUSSION

2.1. Design and Synthesis of CL-Targeting Dimeric Bundle Peptide Library.
Previously reported mitochondrial-specific SS peptides contain β-sheet secondary structures[10,12] and exhibit amphipathic characteristics. However, the relatively short distance (7 Å) between the hydrophilic and hydrophobic moieties of aa in these peptides[23] is insufficient to create hydrophobic interactions with lipid moieties in phospholipids, such as CL, following initial electrostatic interactions between their hydrophilic moieties and phosphate groups. Additionally, only two charged sites exist in SS-31 that participate in a 1:1 interaction with CL.[24] We hypothesized that, in contrast to shorter peptides, α-helical peptides consisting of 10 amino acids may generate bundles without the disadvantages associated with CL binding. Specifically, the amphipathic α-helical structures of 10-aa peptides, with a greater distance (11.3 Å) between hydrophilic and hydrophobic sites, may exhibit a stronger hydrophobic interaction with the fatty acid side chains of CL (Figure 1a). Furthermore, if the α-helical peptide contains more than four positively charged sites in its helix, then it may have avidity for multiple CL molecules. Based on these hypotheses, we designed a series of α-helical peptides and assessed their mitochondrial targeting and inhibition of mitochondrial dysfunction. Various numbers (1−4) of the noncanonical hydrophobic moiety, namely, Cha, were incorporated into the typical helical peptide monomer LR10 to generate stronger hydrophobic interactions with the fatty acid side chains of CL (Figure 1b). To simplify the screening process, 15 monomeric peptides were synthesized in either acetyl-capped or fluorescence-labeled forms (Table S1). Subsequently, the dimeric bundle library was constructed through air oxidation between two versions of monomers, resulting in 15 dimeric bundles for enhancing cell permeability (Figures 1c−e and S1; Tables S2 and S3).
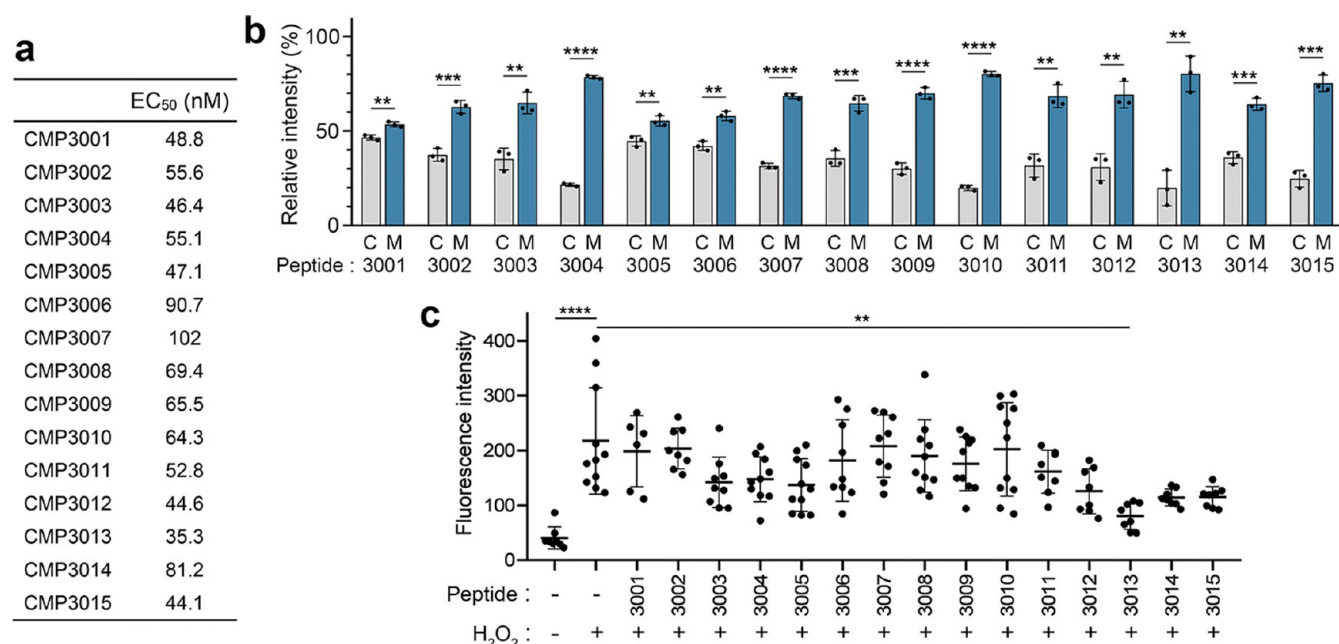
Figure 2. Cell permeability and mitochondrial targeting of Cha-containing peptides. (a) Comparison of the cell permeability of the synthesized TAMRA-labeled dimeric bundle peptides. (b) Mitochondrial fractionation of TAMRA-labeled dimeric bundle peptides. C: cytosolic fraction; M, mitochondrial fraction. (c) Comparison of intracellular ROS inhibition for each member of the TAMRA-labeled dimer bundle peptide library. Increased ROS levels were caused by the H_2O_2 (0.5 mM) treatment.

2.2. Selection of an Effective "Bundle" Peptide through Assessment of Cell-Penetrating and ROS-Reducing Abilities.

Prior to the main screening process, cell penetration of the fluorescence-labeled dimeric bundle library was assessed in HeLa cells by determining effective concentration 50 (EC_{50}) values. As expected, the fluorescence intensity analysis revealed that all dimeric bundles entered the cells at concentrations in the two-digit nanomolar range. Among the library members, CMP3013, which contained three Cha side replacements at positions 1, 5, and 8, exhibited the highest cell penetration ability (EC_{50} = 35 nM; Figures 2a, S2, and S3).[25] Subsequently, the peptide bundles underwent a two-step screening process. First, to evaluate mitochondrial specificity, we determined the fractionation of each peptide into the organelle, with 53−80% of the peptides showing substantial localization in the mitochondria (Figures 2b and S4). Notably, a few peptides (CMP3004, 3010, and 3013) exhibited the highest fractionation in the mitochondria. Second, we conducted a screening process to determine the ability of the peptides to ameliorate mitochondrial dysfunction by reducing ROS levels induced by H_2O_2 treatment in HeLa cells. As shown in Figure 2c, treatment with CMP3013 resulted in the lowest ROS levels (Figure S5). Additionally, we examined the effects of LR10 on mitochondria. Despite its relatively high cell permeability and mitochondrial specificity, LR10 did not exhibit biological activity and failed to decrease H_2O_2-induced ROS generation in cell-based assay (Figure S6).

2.3. CMP3013 Selectively Enters and Restores the Damaged Mitochondria.

The two-step screening study prompted further evaluation of the Cha-modified α-helical peptide dimeric bundles, particularly CMP3013. Although fluorescence analysis showed a high percentage of CMP3013 in the mitochondria of HeLa cells, the correlation factor with MitoTracker was unexpectedly low, particularly in the extended form of mitochondria (Figure 3a). Interestingly, CMP3013 preferentially colocalized with donut- or bulge-shaped mitochondria,[26,27] indicating its binding preference for damaged mitochondria (Figure 3a,b). Colocalization experiments with a fluorescence-labeled fission-initiating protein, namely, Drp1, confirmed the preference of CMP3013 for damaged mitochondria (Figure S7) that required fission.[28] A time-dependent increase in the correlation of CMP3013 with MitoTracker was observed in HeLa cells damaged by carbonyl cyanide m-chlorophenylhydrazone (CCCP) treatment,[29,30] further supporting the preferential binding of CMP3013 to damaged mitochondria (Figure 3c). Cells treated with CCCP and CMP3013 showed improved survival compared with those treated with CCCP alone (Figure S8). Notably, CMP3013 specifically targets CLs in the IMM and binds preferentially to exposed CLs rather than those protected by other proteins in the cristae organizing system[31] or functional complexes.[32] Thus, when proteins completely protect the IMM surface, CMP3013 cannot bind to CL (Figures 3a−c, S7, and S8).

Cell-based assays were conducted to evaluate the effects of CMP3013 on ROS and ATP levels in mitochondria (Figure 3d−f). Various mitochondrial damaging agents were used, and the results revealed that CMP3013 dose-dependently inhibited ROS production, increased ATP production, and increased mitochondrial membrane potential irrespective of the damaging condition (Figure S9). Mitochondrial membrane potential was increased following treatment with CMP3013 (Figure 3g). Therefore, the preservation of mitochondrial function by CMP3013 may be attributed to its ability to protect the cristae structure. Transmission electron microscope (TEM)-based analysis (Figure 3h) of damaged HeLa cells revealed that CMP3013 preserved long and extended cristae similar to the untreated group, whereas H_2O_2-damaged cells showed a significant reduction in long cristae. Notably, a low concentration of CMP3013 (10 nM) exhibited efficacy in these experiments, as well as in previous cell-based assays.

2.4. Mechanism of Cell Penetration and Intracellular Localization of CMP3013.

The mechanism of CMP3013's
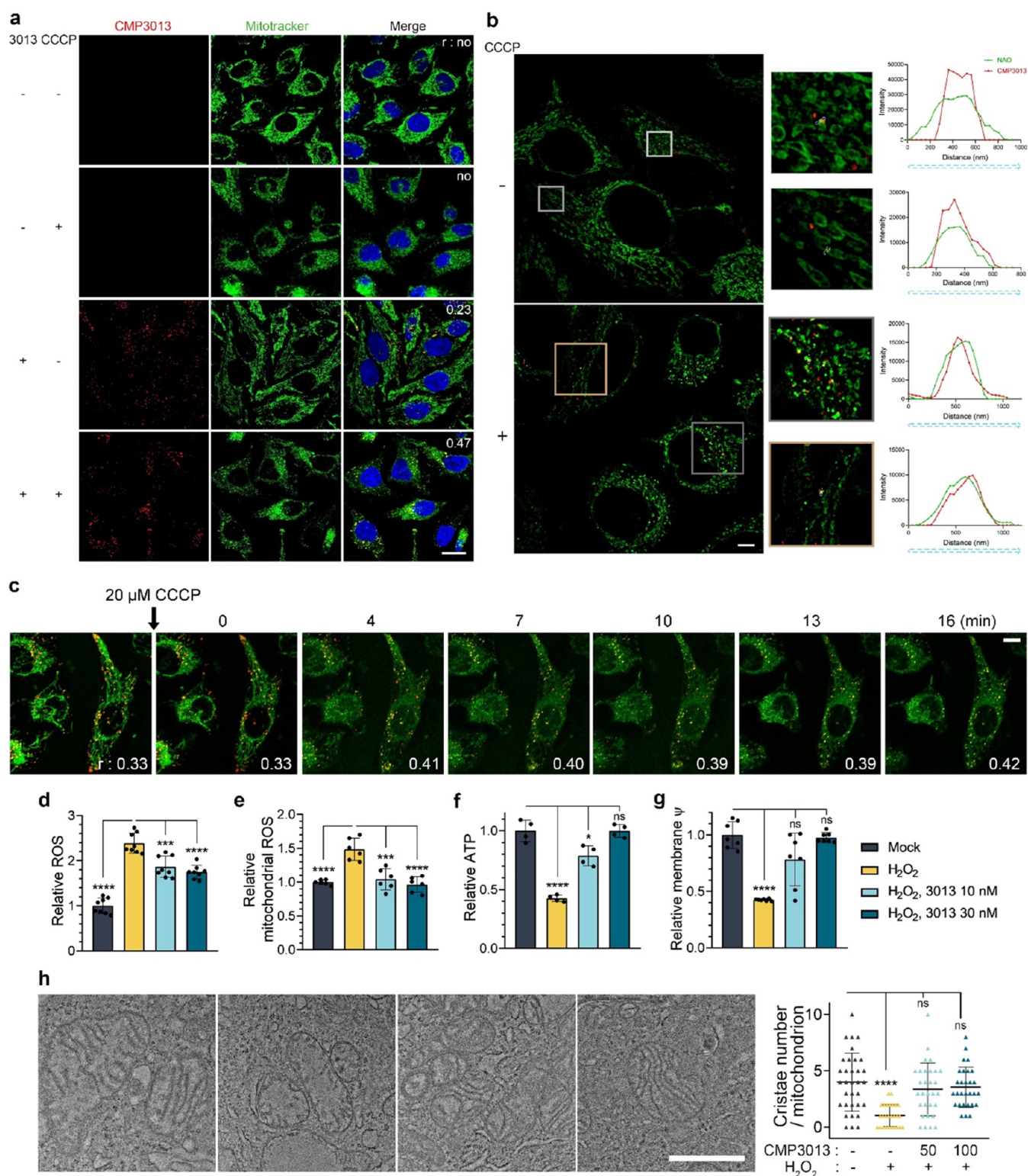
Figure 3. CMP3013 is predominantly localized to damaged mitochondria, maintains mitochondrial function, and protects mitochondria cristae in oxidative-damaged cells. (a) TAMRA-CMP3013 (3013; 100 nM) was added to HeLa cells for 3 h, which were then stained with MitoTracker to visualize the mitochondria. Mitochondrial damage was induced by a 20 μM CCCP treatment (30 min). Pearson r values were calculated to assess the correlation between red (CMP3013) and green (MitoTracker) signals. Scale bar: 20 μm. (b) Super-resolution images confirming the localization of CMP3013 to damaged mitochondria. HeLa cells treated with 100 nM TAMRA-CMP3013 (3 h) were stained with NAO to label cardiolipin. CMP3013 localized to the extended form of mitochondria in the absence of CCCP. In the presence of 20 μM CCCP (30 min), CMP3013 colocalized with damaged mitochondria. The degree of overlap between the NAO and CMP3013 signals is indicated by light blue arrows. The right panel graphs show the correlation between the green (NAO) and red (CMP3013) signals. The x-axes of the graphs represent the start and end (nanometers) of the arrow. Scale bar: 5 μm. (c) Time-lapse images confirm CMP3013 relocation to damaged mitochondria. HeLa cells treated with 100 nM TAMRA-CMP3013 (3 h) and MitoTracker were imaged using a confocal microscope. Mitochondria were damaged by the CCCP treatment. As CCCP-induced damage progressed, the overlap between mitochondria and CMP3013 increased, as indicated by the

Figure 3. continued

increase in Pearson r values. Scale bar: 10 μm. In addition, refer to Supplementary Movie 1. (d, e) CMP3013 inhibits total ROS (d) and mitochondrial ROS (e) production. Peptide pretreated (3 h) cells were exposed to H_2O_2 (0.5 mM) for 30 min. Signals were acquired by using a microplate reader (TECAN). (f) CMP3013 restores ATP production. Peptide pretreated (3 h) cells were treated with 1 mM H_2O_2 for 1 h. (g) CMP3013 preserves the mitochondria membrane potential (ψ) from H_2O_2 exposure. Cells were treated with the peptide (3 h) followed by treatment with 1 mM H_2O_2 for 1 h. (h) Transmission electron microscopy (TEM) images of HeLa cells obtained after various treatments. First from the left, Mock; second, 0.5 mM H_2O_2 treatment; third, 50 nM CMP3013; and fourth,100 nM CMP3013 treatment for 2 h, followed by 0.5 mM H_2O_2 treatment for 2 h. For the graph, cristae of >0.5 μm in length were counted from at least 50 independent images of mitochondria. Scale bar: 1 μm. Refer to the Methods section for experimental details.

cell penetration and its fate within the cell were investigated. Endocytosis, particularly the cholesterol-mediated pathway, is likely involved in the cell penetration of CMP3013 (Figure 4a). Colocalization studies with an endosome marker showed that only a small portion of CMP3013 was present in the endosomes, suggesting successful escape from the endosome Some CMP3013 localized to the lysosomes (Figure 4b). We also investigated whether mitochondrial damage affects the accumulation of the peptide in the lysosome (Figure 4c).[33] Regardless of the presence of CCCP, the amount of peptide in the lysosome remained consistent (0.29 and 0.30, respectively). These results indicate that CMP3013 does not promote mitophagy,[34] which is an important pathway for removing dysfunctional mitochondria. In contrast, the portion of CMP3013 in the cytosol significantly increased in the presence of CCCP (0.43) compared with that in its absence (0.08; Figure 4d). These findings provide further evidence that CMP3013 specifically targets damaged and exposed CL-containing IMM.

2.5. CMP3013 Specifically Binds to and Remains in the CL- or Pathogenically Remodeled CL-Rich Membrane. To investigate the specificity of CMP3013 toward a CL-rich membrane, we employed two model systems that mimic the IMM. In the first approach, we used a sensor chip based on surface plasmon resonance. CMP3013 exhibited a 50% greater response when interacting with a 10% CL-rich membrane containing 1-palmitoyl-2-oleoyl-*sn*-glycero-3-phosphocholine (POPC)/1-palmitoyl-2-oleoyl-*sn*-glycero-3-phosphoethanolamine (POPE) compared with an analogue containing only POPC/POPE. However, dissociation of the peptide from the CL-containing membrane was not observed due to the destruction of the membrane under all dissociation conditions employed, suggesting a strong interaction between CMP3013 and the CL-containing membrane (data not shown). In the second model system, liposomes were fabricated using a liposome formation technique.[35,36] Fluorescence-labeled CMP3013 associated nearly 10-fold faster and emitted 2-fold greater final fluorescence intensity in response to a 10% CL-rich liposome containing POPC/POPE compared with a liposome containing only POPC/POPE (Figures 5a,d,e and S10). The dissociation of the peptide from the CL-rich membrane containing POPC/POPE, as determined via a competition assay with nonlabeled peptides, was approximately 10-fold slower compared to the CL-free membrane. The rapid association is likely attributed to interactions between the positively charged groups in CMP3013 and the negatively charged phosphate moieties in CLs, whereas both charged and hydrophobic interactions between the lipid components of the two molecules contribute to slow dissociation (Figure 5a,b,d,e).

To determine whether CMP3013 binds to pathogenically altered IMM, two additional artificial membranes were created.

The first consisted of POPC/POPE (2:1) liposomes with varying CL contents (0−20%) (Figure 5c), whereas the second contained liposomes with 10% dilysoCL (DLCL) along with POPC/POPE liposomes (Figure 5a). The results showed that the monomeric form of CMP3013 (3013m) was effectively bound to liposomes with 5−10% CL compared with those containing 20% CL (Figure 5c). The peptide was also bound to liposomes containing 10% DLCL similar to those with 10% CL (Figure 5a). These findings suggest that CMP3013 binds to CL-deficient or CL-damaged membranes and may counteract pathogenic CL remodeling in the IMM. Super-resolution images of mitochondria cotreated with fluorescence-labeled CMP3013 and nonyl acridine orange (NAO) revealed that the peptide's final destination was the CL-rich IMM, exhibiting complete colocalization with CL-specific NAO dye (Figure 3b). The colocalization was more pronounced in the presence of CCCP, further confirming the peptide's preference for damaged IMM where CL is exposed and readily available for binding.

2.6. Low-Dose CMP3013 Treatment in a Colistin-Induced Nephrotoxicity Model Protects Mitochondrial Structure and Function. Based on the cell-based assay results and *in vitro* targeting studies mentioned above, we evaluated the efficacy of CMP3013 in a mouse model of colistin nephrotoxicity.[37,38] This model was chosen owing to its reversible acute indication, allowing for the promotion or protection of mitochondrial function using minimal doses. Prior to conducting the animal experiment, we confirmed that CMP3013 exhibited superior cell permeability and selective targeting of mitochondria in human tubular epithelial cells (hTECs). Consistent with our findings in HeLa cells, CMP3013 showed a higher level of localization in damaged mitochondria (Figure S11a−c). Super-resolution microscopy images further confirmed reliable colocalization patterns of CMP3013 with bulge-shaped mitochondria compared with extended form (Figure 6a). Measurement of intracellular ROS levels revealed that CMP3013 effectively inhibited ROS production in hydrogen-peroxide-stimulated cells at low nanomolar concentrations (Figure 6b). Additionally, CMP3013 preserved mitochondrial membrane potential and restored ATP production after exposure to various mitochondrial damaging agents (Figures 6c,d and S11d). Assessment of mitochondrial oxygen consumption rate (OCR) and extracellular acidification rate (ECAR) indicated that CMP3013 improved mitochondrial basal respiratory and maximum respiratory levels between 40 and 60 min in a dose-dependent manner as well as glycolytic ATP production [measured as the glycolytic proton efflux rate (PER): glycoATP production rate (pmol ATP/min) = glycoPER (pmol H^+/min), respectively. These findings indicate that CMP3013 positively impacts mitochondrial function, improving overall quality (Figure 6e).
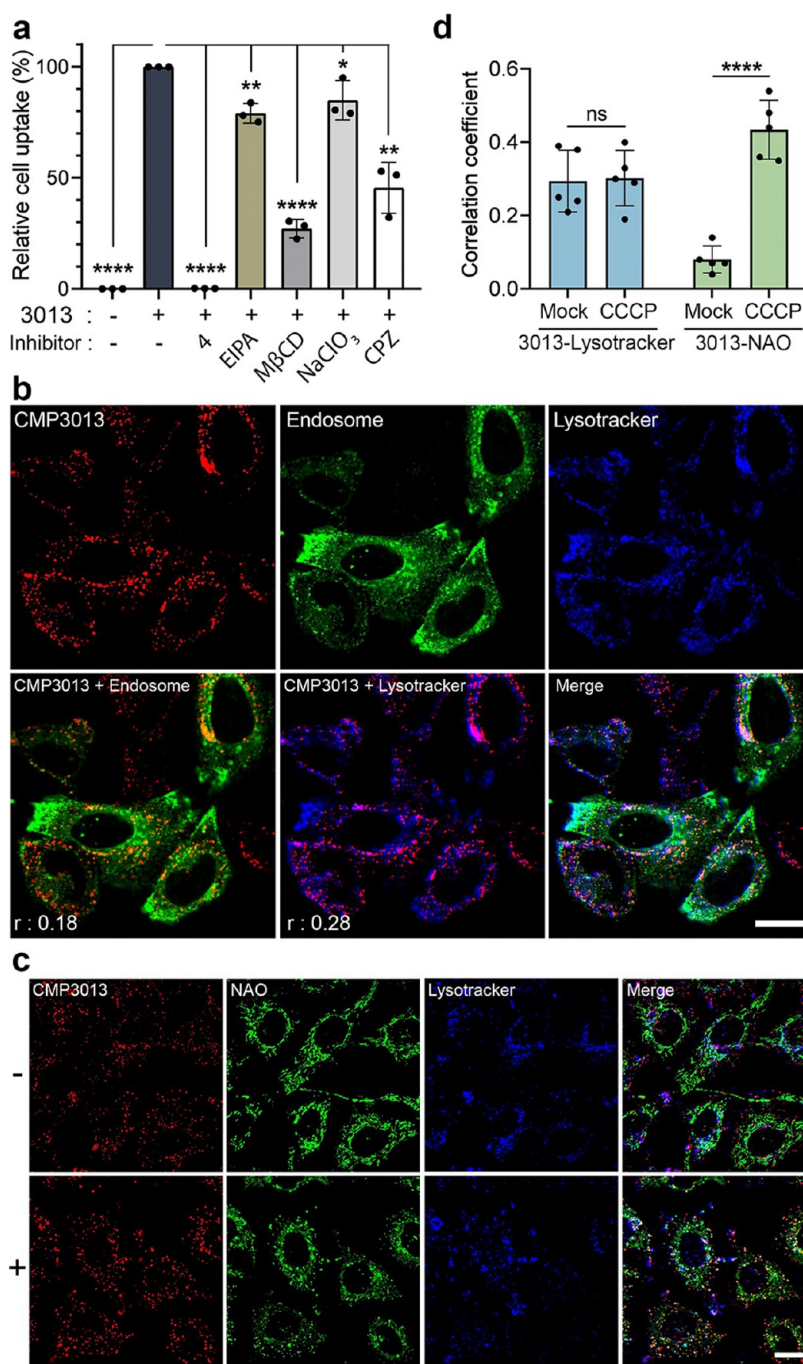
Figure 4. Cell entry mechanisms of CMP3013 and its eventual fate in cells. (a) Endocytosis mechanism of CMP3013. HeLa cells were pretreated with various inhibition conditions for 30 min: prechilling at 4 °C (ATP dependency), 5-(N-ethyl-N-isopropyl)amiloride (EIPA, macropinocytosis), methyl-β-cyclodextrin (MβCD, for cholesterol depletion), sodium chlorate (NaClO$_3$; proteoglycan-dependent pathway), and chlorpromazine (CPZ; clathrin-mediated endocytosis). The cells were incubated for 3 h with 100 nM TAMRA-CMP3013 (3013) followed by fluorescence-activated cell sorting (FACS) analysis. (b) HeLa cells expressing endosome markers (16 h) were treated with TAMRA-CMP3013 (100 nM; 3 h) and LysoTracker (50 nM; 1 h). r: Pearson correlation value. Scale bar: 20 μm. (c) CL-specific targeting (using 100 nM NAO; 1 h) of TAMRA-CMP3013 (100 nM; 3 h) in the absence (−) or presence (+) of CCCP (20 μM; 30 min). Scale bar: 20 μm. (d) Comparison of Pearson r values from (c) images; (blue bars) CMP3013-LysoTracker and (green bars) CMP3013-NAO. Five independent fluorescence images (magnification: 63×) were analyzed for each condition.

Efficacy tests of CMP3013 were performed on a CIN mouse model. Mice treated with CMP3013 (1 mg/kg) showed a significant reduction in blood urea nitrogen (BUN) and creatinine excretion for up to 7 days compared with CIN mice (Figure 6f). CMP3013-treated mice also exhibited reduced levels of acute tubular necrosis, tubular casts, tubular dilation, and renal fibrosis. Furthermore, the expression levels of NGAL (a kidney injury marker), P-21 (a cell cycle arrest and apoptosis marker), 8-OHdG (a biomarker for oxidative DNA lesions), and cytochrome C (a mitochondrial apoptotic marker) were decreased, whereas the expression of SOD-1 (an antioxidant enzyme) was increased, in CMP3013-treated
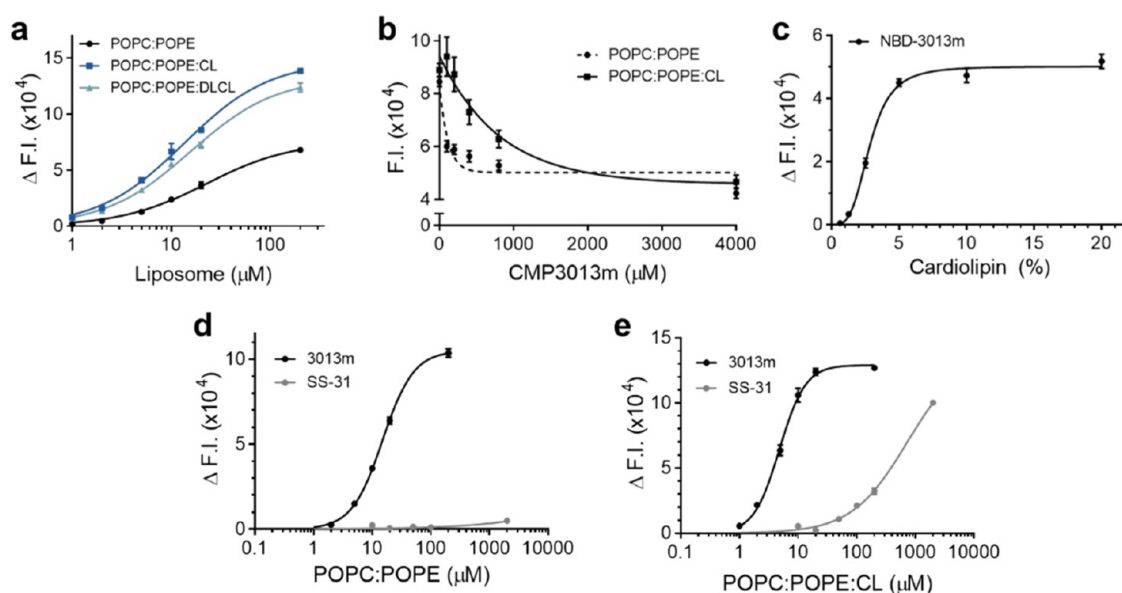
Figure 5. CMP3013 monomer interacts strongly with CL-containing membranes fabricated with liposomes. (a) Three types of liposomes, POPC/POPE (2:1) (black), POPC/POPE (2:1) with 10% CL (blue), and POPC/POPE (2:1) with 10% DLCL (pale blue), were added to 1 μM NBD-labeled CMP3013 monomer (NBD-3013m). (b) After the addition of liposomes to 1 μM NBD-3013m, excess CMP3013 monomer (CMP3013m) was administered. (c) CMP3013m exhibits CL-dependent binding. Liposomes with various CL proportions (0−20%) were incubated with NBD-3013m. ΔF.I. represents the change in fluorescence intensity. 6-NBD: 6-(7-nitrobenzofurazan-4-ylamino)hexanoic acid: (d, e) POPC/POPE (2:1) liposome (d) or POPC/POPE (2:1) with 10% CL (e) were added to 1 μM NBD-3013m (black) or NBD-SS-31 (gray) (n = 3).

mice compared with CIN mice (Figures 6g and S12). Survival rate analysis revealed that CMP3013-treated mice had the highest survival rate, similar to that of the control group and significantly longer than that of CIN mice (Figure 6f). Notably, examination of kidney sections showed that CMP3013 preserved the cristae structure and maintained compact cristae in the mitochondria, protecting them from colistin-induced damage (Figure 6h). These results indicate that CMP3013 restores kidney function by preventing mitochondrial dysfunction associated with kidney failure.

2.7. CMP3013 Demonstrates Efficacy in Protecting the Kidneys from Acute Renal Injury in a Mouse Model by Improving Mitochondrial Function. To evaluate the effect of CMP3013 in a bilateral ischemia-reperfusion injury (IRI) mouse model, known for inducing severe hypoxia and high mortality, we first assessed the impact of CMP3013 on cell survival following oxidative stress in hTECs. Interestingly, even at low concentrations, CMP3013 effectively inhibited apoptosis in hydrogen peroxide−exposed cells (Figure S13a,b,d). Furthermore, CMP3013 alleviated cell cycle inhibition (p16 and p21) caused by oxidative stress and suppressed proinflammatory cytokine transcription (IL-1β and IL-18) (Figure S13b,c), suggesting its beneficial effects on cell survival under oxidative stress conditions.

In IRI mice, administration of low-dose CMP3013 resulted in a reduction in serum BUN and creatinine levels (Figure 7a,b). Immunohistochemistry analysis of the damaged kidney tissue revealed that the CMP3013-treated group exhibited less tubular damage, cast formation, and inflammatory cell infiltration (Figures 7c and S14). Furthermore, the CMP3013-treated group showed decreased levels of NGAL and cytochrome C, along with an increase in SOD-1 expression (Figures 7c,d and S14). Additionally, CMP3013 administration in IRI mice resulted in upregulated expression of NQO-1 and SOD-1 mRNA, which are essential mitochondrial antioxidant enzymes.[39,40] It also induced elevated transcription of IL-10, an

antioxidant and anti-inflammatory cytokine,[41] and ATP6 mRNA, associated with the function of the mitochondrial electron transport complex channel 5[42] (Figure 7e). To confirm the ameliorative effects of CMP3013 on impaired kidneys, we reversed the order of treatment for CMP3013 and IRI. Unexpectedly, the application of 1 mg/kg CMP3013 after IRI led to a decrease in serum BUN and creatinine concentrations (Figure 7f). These findings indicate that CMP3013 exerts a renal protective effect in an acute kidney injury mouse model through enhancement of mitochondrial function.

3. CONCLUSIONS

The mitochondrial-specific peptide CMP3013 has several advantageous characteristics that make it a promising candidate for therapeutic use. First, owing to its origin from a cell-penetrating dimeric bundle peptide, CMP3013 efficiently enters cells at low nanomolar concentrations, exhibiting high cell permeability in HeLa and hTEC cells. Second, the peptide selectively targets the mitochondria, with approximately 80% of it localizing in this organelle, minimizing the presence of CMP3013 in the cytosol and reducing the risk of side effects. Third, CMP3013 demonstrates a preferential binding affinity for CL, the predominant phospholipid in the IMM. This binding capability enables the preservation of the cristae structure and ensures the stability and activity of functional proteins. Notably, CMP3013 exhibits a strong avidity for multiple CL molecules, resulting in a more robust interaction than expected for a 1:1 complex. Consequently, the dissociation of the peptide from the IMM is slow, resulting in a more potent and pronounced effect. The complete colocalization of CMP3013 with the CL-specific dye NAO in damaged IMM further supports its retention in CL-rich regions. Consequently, CMP3013 effectively curtails ROS production, which is exacerbated in leaky IMM, even at low
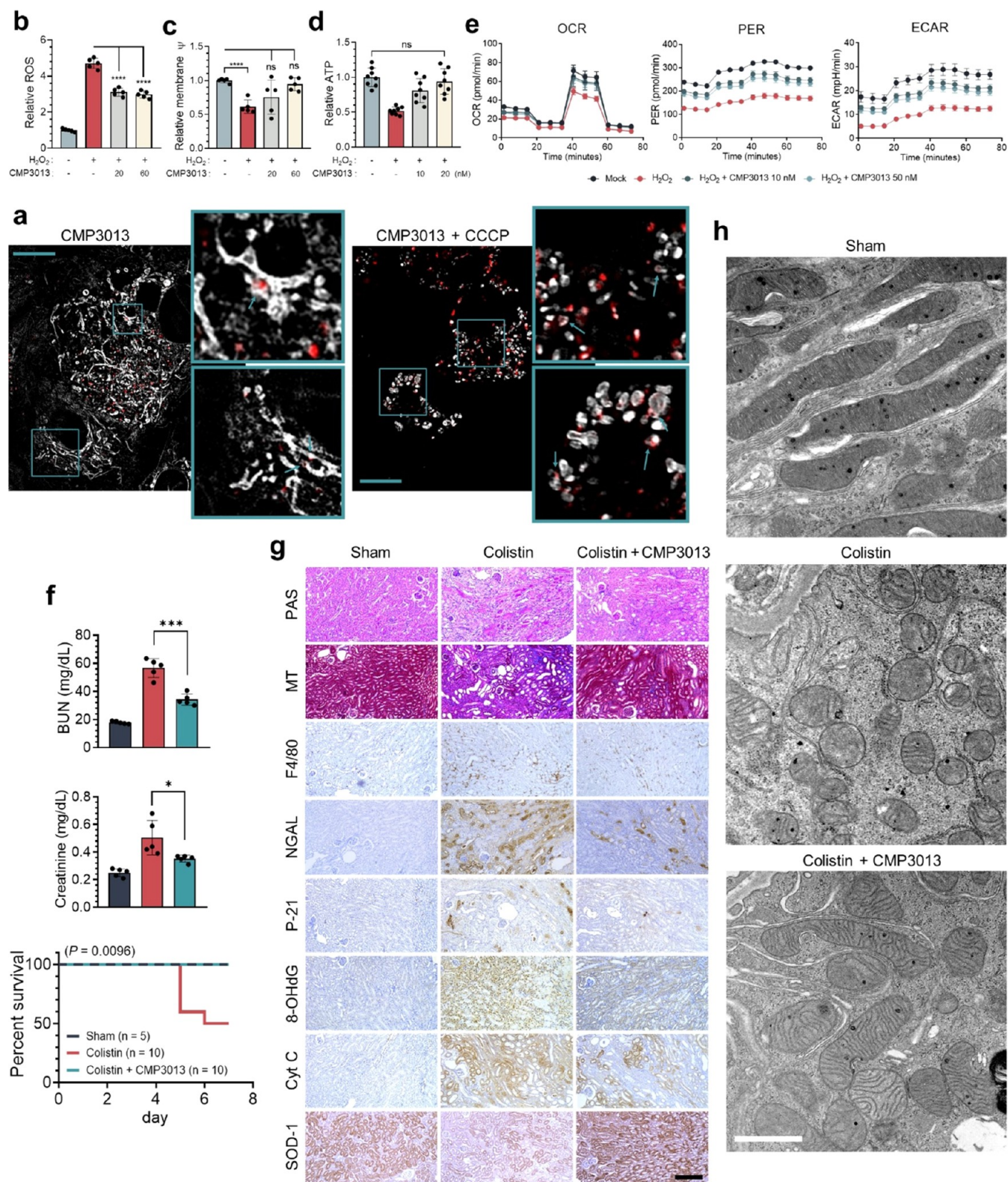
Figure 6. CMP3013 exerts therapeutic effectiveness by protecting mitochondrial cristae and function in a mouse model of colistin-induced kidney damage. (a, b) CMP3013 inhibits ROS generation (a) and preserves mitochondrial membrane potential (b) in hTECs. Cells were incubated with the peptide (3 h) and treated with H_2O_2 (1 mM; 30 min). Signals were obtained using a microplate reader. (c) ATP levels were maintained in CMP3013-treated (3 h) hTECs, which were affected by H_2O_2 (0.5 mM; 1 h). (d) Seahorse assay results showing OCR (H_2O_2 vs Mock ***, H_2O_2 vs H_2O_2 + CMP3013 10 nM ***, and H_2O_2 vs H_2O_2 + CMP3013 50 nM *), ECAR (H_2O_2 vs Mock ***, H_2O_2 vs H_2O_2 + CMP3013 10 nM ***, and H_2O_2 vs H_2O_2 + CMP3013 50 nM **), and PER (H_2O_2 vs Mock ***, H_2O_2 vs H_2O_2 + CMP3013 10 nM ***, and H_2O_2 vs H_2O_2 + CMP3013 50 nM **). Measurements indicate cellular respiration and glycolysis in hTECs following exposure to H_2O_2 and CMP3013 (10 and 50 nM). n = 36 (Mock 6, H_2O_2 6, H_2O_2 + CMP3013 10 nM 6, and H_2O_2 + CMP3013 50 nM 6). (e) hTECs were incubated with TAMRA-CMP3013 (100 nM; 3 h), and super-resolution images were acquired. White represents NAO signals; red represents CMP3013. Scale bar: 10 μm. (**f–h**)

Figure 6. continued

Colistin-induced kidney injury mice were treated with colistin (20 mg/kg, SC, daily) and CMP3013 (1 mg/kg, IP, daily). (f) (Left) On day 7, BUN and creatinine levels in the blood were measured. $n = 5$/group (mean ± standard error of the mean (SEM)). (Right) Kaplan−Meier survival curve for the indicated groups. The log-rank (Mantel−Cox) test was used for statistical analysis: $*P < 0.05$, $**P < 0.01$, and $***P < 0.001$. (g) Mice were treated with colistin (20 mg/kg, SC, daily) and CMP3013 (1 mg/kg, IP, daily). At 7 days, periodic acid-Schiff stain (PAS), Masson's trichrome (MT), F4/80, NGAL (neutrophil gelatinase−associated lipocalin), P-21, 8 hydroxyguanosine (8-OHdG), cytochrome C (Cyt C), and superoxide dismutase (SOD-1) expression in the damaged kidney tissue were determined using immunohistochemistry. Expression levels of cytochrome C and NGAL were decreased in CMP3013-treated mice compared with colistin-induced nephrotoxicity (CIN) mice. Magnification: 100×. Scale bar: 100 μm. (h) TEM images were acquired from kidney sections. Scale bar: 1 μm.
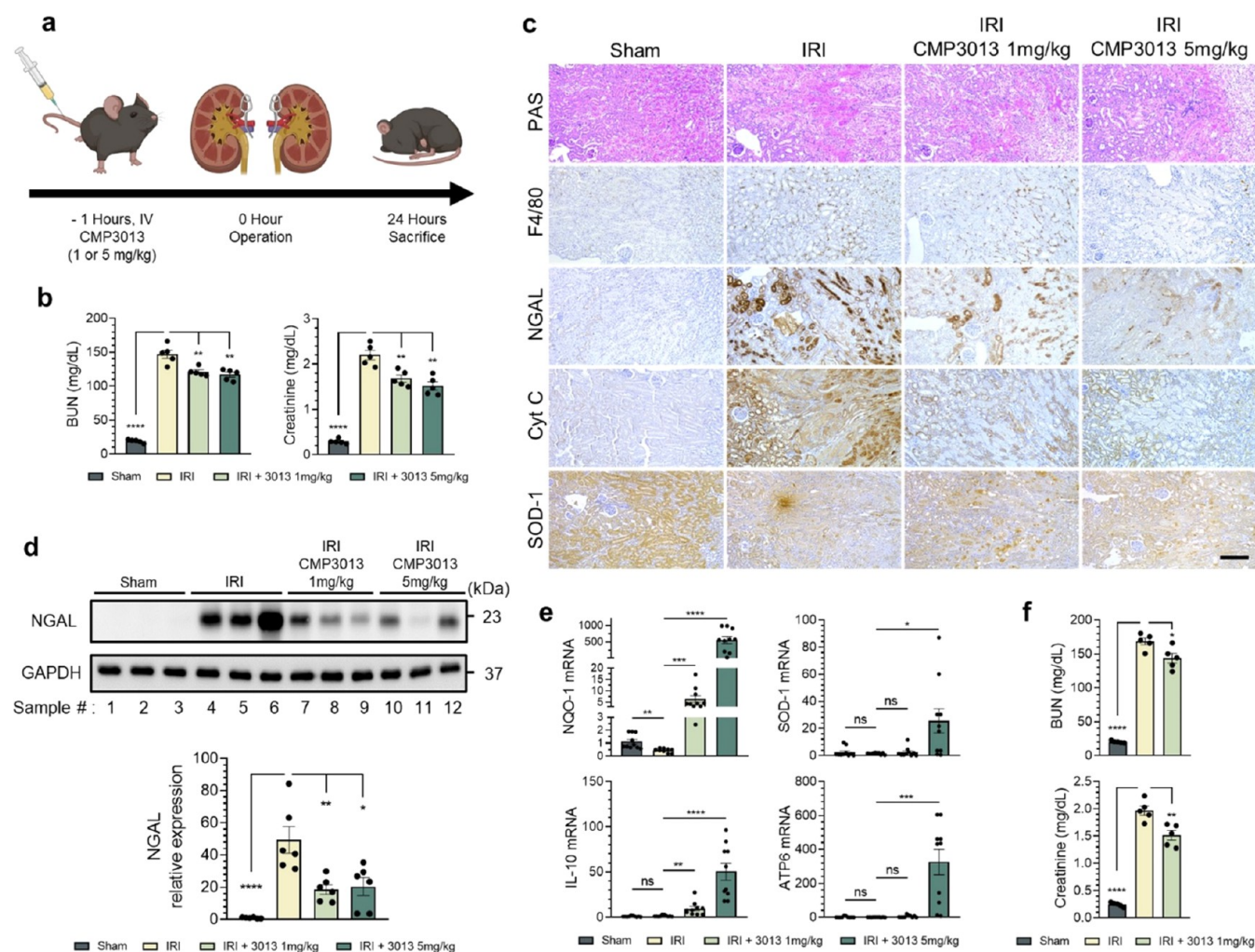
Figure 7. CMP3013 promotes renal function recovery in a mouse IRI model by enhancing mitochondrial functions. (a) Schematic representation of the *in vivo* IRI model. (b) Creatinine and BUN were assessed 24 h after IRI induction, respectively. Mean ± SEM (c) Histological changes in kidney sections after CMP3013 administration were evaluated. $n = 10$/group. Cyt C: cytochrome c. Magnification: 100×. Scale bar: 100 μm. (d) Western blot analysis of NGAL in renal tissue was performed to measure the effects of different CMP3013 treatments. $n = 6$/group. (e) Quantitative analysis of antioxidant mRNA profiles. Animals were sacrificed 24 h post-IRI. (f) One hour after the introduction of IRI, mice were administered CMP3013. BUN and creatinine levels were measured 23 h later. $*P < 0.05$, $**P < 0.01$, and $***P < 0.001$. Data are represented as mean ± SEM. Two-tailed unpaired Student's t test was used for statistical analysis.

concentrations both *in vitro* (<50 nM) and *in vivo* (<1 mg/kg). Notably, no other antioxidant has been found to possess such potent ROS-reducing effects at these low concentrations, as most substances display this effect only at higher concentrations.[43,44]

Mitochondria possess various defense mechanisms to counteract ROS;[45] however, proximal ROS accumulation primarily occurs in the IMM, where pathogenic CL remodeling takes place. This remodeling process involves physicochemical alterations, such as increased peroxidation and loss of acyl chains in CL, elevated unsaturated content and length of acyl chains, and reduced CL content. Oxidation and removal of acyl chains give rise to monolysoCL or DLCL, and the recruitment of longer and more unsaturated acyl chains leads to the generation of bulkier CL molecules.[46] The presence of unsaturated acyl chains containing allylic hydrogens prone to oxidation further exacerbates oxidative remodeling. Additionally, the formation of a leaky membrane results in functional CL synthase loss and a subsequent decline in the CL content. Our findings demonstrate that CMP3013 exhibits strong

binding affinity to artificial IMMs that mimic the effects of pathogenic CL remodeling, including membranes containing 10% DLCL or reduced CL levels (from 20 to 5%) (Figure 5). These results indicate that CMP3013 can rescue mitochondrial dysfunction resulting from CL peroxidation or remodeling, surpassing the limitations of gene expression attenuation.[47] Moreover, these findings highlight the capability of CMP3013 to inhibit pathological CL remodeling in the IMM at nanomolar concentrations, an effect that cannot be accomplished by other known molecules.

The images revealing the low correlation between CMP3013 and the extended form of mitochondria, along with the higher correlations with donut- and bulge-shaped organelles, are of great importance (Figure 3a). These observations suggest that CMP3013 selectively enters damaged mitochondria, where CL is less protected by cristae or functional proteins. Thus, it is anticipated that CMP3013, even in small quantities, may effectively inhibit CL remodeling and rescue damaged mitochondria while having minimal impact on functional mitochondria. This characteristic of the peptide indicates that nanomolar concentrations can achieve reduced toxicity while providing sufficient protection for mitochondrial function, including ATP generation and increased mitochondrial potential.

In summary, the findings of this study demonstrate that the α-helical amphipathic peptide CMP3013 exhibits a preference for binding to aberrant and damaged mitochondria, promoting the retention of IMM and cristae structures that are disrupted by damaging treatments in AKI induced by IRI and colistin nephrotoxicity. CMP3013 facilitates the reduction of NGAL and cytochrome C expression, thereby maintaining mitochondrial homeostasis, scavenging ROS, and increasing the ATP supply. A particularly encouraging outcome from both the *in vitro* and *in vivo* animal model studies is the observation that positive effects are achieved at remarkably low concentrations of CMP3013 (1 mg/kg). Considering that mitochondrial homeostasis involves biogenesis and mitophagy, the repair of all defective mitochondria is not essential,[48] as a small portion of damaged mitochondria repaired by CMP3013 should be adequate to restore normal tissue function. The comprehensive analysis presented here suggests that CMP3013 markedly enhances survival and tissue recovery in various mouse models by reducing inflammation (Figures 6, 7, and S15), thereby positioning it as a potential therapeutic agent against mitochondrial diseases,[49,50] including chronic kidney diseases following AKI.

4. EXPERIMENTAL SECTION

4.1. Peptide Synthesis. Peptides were synthesized using a standard 9-fluorenylmethyloxycarbonyl (Fmoc) solid-phase peptide synthesis method using *N,N*-dimethylformamide (DMF) on an SPS microwave peptide synthesizer (Discover, CEM) as previously described.[13] Rink amide MBHA resins were deprotected with 20% (v/v) piperidine in *N,N*-dimethylformamide. Fmoc-protected aa were coupled in the presence of *N,N*-diisopropylethylamine (DIPEA) and (benzotriazol-1-yloxy)tripyrrolidinophosphonium hexafluorophosphate (PyBOP). Resins were washed several times with DMF and dichloromethane (DCM) with gentle shaking. Deprotection and coupling were repeated until the desired peptide was synthesized. After the addition of the last amino acid, the N-terminus of the peptide was modified. Acetylation was performed by adding acetic anhydride and 1-hydroxybenzotriazole hydrate (HOBt) to DMF/DCM (9:1). 5-Carboxytetramethylrhodamine was conjugated in the presence of *O*-(1*H*-6-chlorobenzotriazole-1-yl)-1,1,3,3-tetramethy-

luronium hexafluorophosphate, HOBt, and DIPEA using DMF. 6-(7-Nitrobenzofurazan-4-ylamino)hexanoic acid (C6-NBD) was labeled with PyBOP and DIPEA in DMF.[51] The synthesized peptides on the resins were cleaved using a cleavage cocktail [containing trifluoroacetic acid (TFA)/1,2-ethanedithiol (EDT)/water/triisopropylsilane in a ratio of 94:2.5/2.5/1 (v/v)]. To precipitate the cleaved peptides, a 1:1 (v/v) mixture of *n*-hexane and diethyl ether was added. The precipitated peptides were then centrifuged at 5000 rpm for 15 min, and the resulting pellet was dissolved in dimethyl sulfoxide (DMSO). For purification, high-performance liquid chromatography was employed. The mobile phase consisted of deionized water with 0.1% TFA (v/v) (buffer A) and acetonitrile (ACN) with 0.1% TFA (v/v) (buffer B). A Zorbax C18 column (3.5 μm, 4.6 mm × 150 mm) was used as the stationary phase. The gradient method used was as follows: 5% B for 5 min, followed by a linear gradient from 5 to 70% B from 5 to 30 min and from 70 to 100% B from 30 to 40 min. The flow rate was set at 1.0 mL/min. After purification, the peptides were lyophilized and dissolved in an appropriate solvent. To determine the molecular weights of the peptides, matrix-assisted laser desorption/ionization time-of-flight (MALDI-TOF) mass spectrometry (Bruker) was performed. All peptides used in this study were confirmed to have over 95% purity by reversed-phase HPLC analysis.

4.2. Peptide Dimerization. The lyophilized peptide was dissolved in 0.1 M ammonium bicarbonate. In some cases, ACN was added up to 40% (v/v) to increase the peptide solubility. The resulting peptide solution was stirred by using a shaker. After oxidation, the dimerized peptides were purified and lyophilized.

4.3. Cell Culture. HeLa cells were cultured in Dulbecco's modified Eagle's medium (Cytiva, SH30243.01) supplemented with 10% fetal bovine serum (Gibco, 16000-044) and antibiotics (Gibco, 15240-062). Kidney biopsy samples were collected from patients diagnosed with renal cell carcinoma. All experiments involving human subjects were approved by the Institutional Review Board of Seoul National University Hospital, and all patients provided informed consent before enrollment. Human primary renal cells were identified and sorted according to the established protocol.[52] The cells were incubated in a 5% CO_2 humidified incubator at 37 °C.

4.4. Flow Cytometry. HeLa cells (1×10^5) or hTECs (5×10^4) were seeded into a 24-well plate. After 24 h, the peptides were added to the cells, and the cells were further incubated for 3 h. The cells were harvested, washed with phosphate-buffered saline (PBS), and suspended in PBS for fluorescence-activated cell sorting (FACS; BD Accuri) analysis. Fluorescence-positive cells were defined as cells emitting a fluorescence intensity above the maximum intensity of untreated cells. The EC_{50} value represents the concentration of the dimer peptide at which half of the incubated cells entered the corresponding fluorescence-labeled peptide dimer.

4.5. Apoptosis and Necrosis Analysis. hTECs (1×10^5) were seeded into a 6-well plate. After 1 h, CMP3013 was determined by exposing hTECs to H_2O_2 (0.5 mM), and antiapoptosis was measured using an Annexin-propidium iodide (PI) experiment. An annexin V/PI fluorescein isothiocyanate (FITC) apoptosis kit (BD Biosciences) was used to visualize and measure the percentage of apoptosis and necrosis. hTECs were resuspended in 100 μL of binding buffer, and 4.5 μL of FITC-conjugated annexin V (10 mg/mL) and 3.5 μL of PI (50 mg/mL) were added. The cells were incubated for 15 min at room temperature in the dark. BD FACSDiva software (version 8.0; BD Biosciences) was used to collect the measurements.

4.6. Mitochondria Fractionation. The subcellular distribution of peptides was detected using the mitochondria isolation method.[53] TAMRA-labeled peptide was added to 6×10^6 HeLa or 2×10^6 hTECs at the EC_{50} level, and the cells were incubated for 3 h. They were harvested, washed with cold PBS, and suspended in cold IB [30 mM Tris−HCl (pH 7.4), 225 mM mannitol, 75 mM sucrose, and 0.1 mM EGTA]. Homogenization was performed using a precooled Dounce homogenizer until 80−90% of cells were disrupted. Lysed cells were monitored by using light microscopy. The homogenate was transferred to a fresh tube and centrifuged at 600*g* for 5 min at 4 °C. The supernatant was collected and recentrifuged, after which it was then centrifuged at 7000*g* for 10 min at 4 °C. The supernatant

(cytosolic fraction) was then transferred to a new tube. The pellet (mitochondrial fraction) was resuspended in the same volume of cold IB. The fluorescence intensity of each fraction was measured by using a microplate reader (TECAN). The excitation (Ex) and emission (Em) wavelengths were 510 and 570 nm, respectively.

4.7. Confocal Microscopy and Super-Resolution Microscopy. Cells were cultured in glass-bottom dishes (SPL, 200350) and treated with peptides for 3 h. They were then stained with MitoTracker (Thermo Fisher Scientific M7514; 20 μM; 20 min), NAO (Thermo Fisher Scientific A1372; 100 nM; 1 h), Hoechst 33342 (1 μg/mL; 20 min), CellLight early endosomes-GFP (Thermo Fisher Scientific C10586; 2 μL/10,000 cells; 16 h), and/or LysoTracker (Thermo Fisher Scientific L7525; 50 nM; 30 min). After rinsing with PBS, Hanks' Balanced Salt Solution (HBSS) was added to the cells. Microscopic images of the stained cells were captured by using a Zeiss LSM 880 microscope and ELYRA PS.1 system. Super-resolution images were generated by using the structured illumination process with ZEN black software. Pearson r values were calculated by using ImageJ software.

4.8. Measurement of Cellular ROS Levels. Intracellular ROS levels were measured using two methods. First, cells on glass-bottom dishes were treated with TAMRA-labeled peptide at the EC_{50} level for 3 h. The cells were then stained with 2′, 7′-dichlorofluorescein diacetate (H$_2$DCFDA; Sigma 287810; 25 μM; 30 min) washed with PBS, and treated with 500 μM H$_2$O$_2$ in HBSS for 10 min. DCF signals were detected using a confocal microscope, and the green signal intensity was calculated using ZEN blue software. Second, HeLa cells (2×10^4) or hTECs (7×10^3) were seeded into a 96-well plate. After 24 h, the cells were incubated with peptides for 3 h followed by H$_2$DCFDA staining (25 μM; 30 min). After washing twice with PBS, the cells in HBSS were analyzed for ROS levels using a TECAN plate reader at 37 °C (Ex/Em = 485/535 nm).

4.9. Measurement of Mitochondrial ROS and Membrane Potential. HeLa cells (2×10^4) or hTECs (1×10^4) were seeded into a 96-well plate. After 24 h, the cells were stained with MitoSOX (Thermo Fisher Scientific M36008; 5 μM; 10 min) or tetramethylrhodamine ethyl ester (TMRE; Sigma 87917; 600 nM; 15 min). The cells were washed with PBS, and HBSS was added. Fluorescence signals were measured using a TECAN plate reader at 37 °C. MitoSOX Ex/Em = 510/580 nm; TMRE Ex/Em = 525/575 nm.

4.10. Measurement of ATP Levels. Cellular ATP levels were measured using an ATP detection kit (Abcam; ab113849) according to the manufacturer's instructions. Luminescence was measured using a microplate reader (Promega; Gloma× 96 microplate luminometer).

4.11. Seahorse Assay. hTECs were cultured on a Seahorse XF96 cell culture microplate at 37 °C. After 24 h, the OCR and ECAR were measured using the Seahorse XFe 96 extracellular flux analyzer (Agilent, CA). OCR was measured after sequential injections of 2 μM oligomycin, 1 μM carbonyl cyanide 4-(trifluoromethoxy) phenylhydrazone, and 0.5 μM rotenone plus antimycin A to measure the maximal respiration rate. Subsequently, ECAR was determined after sequential injections of 10 mM glucose, 1 μM oligomycin, and 50 mM 2-DG. The PER was measured and calculated using Wave Pro software and Wave Desktop software (Agilent, CA).[54]

4.12. Transmission Electron Microscopy. HeLa cells (1.8×10^7) were fixed with modified Karnovsky's fixative [2% paraformaldehyde and 2% glutaraldehyde in 0.05 M sodium cacodylate buffer (pH 7.2)] at 4 °C for 3 h. After washing with 0.05 M sodium cacodylate buffer (pH 7.2) three times for 10 min each at 4 °C, the specimens were postfixed with 1% osmium tetroxide in 0.05 M sodium cacodylate buffer (pH 7.2) at 4 °C for 2 h. The samples were washed twice with distilled water and stained with 0.5% uranyl acetate at 4 °C overnight. Subsequently, the samples were dehydrated using increasing concentrations of ethanol (30, 50, 70, 80, 90%, and three times at 100% for 10 min each) and treated twice with 100% propylene oxide for 15 min as a transition step. The specimens were then infiltrated with a series of propylene oxide and Spurr's resin (1:1 for 1.5 h, 1:2 for 1.5 h, Spurr's resin only overnight, and once more for 4 h) and embedded in Spurr's resin at 70 °C overnight. Completely polymerized specimens were sectioned by using an ultramicrotome

(MT-X, RMC, Tucson, AZ). Sections were stained with 2% uranyl acetate and Reynolds' lead citrate for 7 min each. The samples were observed using a JEM-ARM200F TEM, and images were acquired. Additionally, kidney mitochondria were observed using a previously described method.[55]

4.13. Plasmid Construction and Transfection. Wild-type Drp1 cDNA was PCR-amplified and inserted into the N-terminus of the *eGFP* gene in the pcDNA3.1- plasmid. Transfection of plasmids was performed using Lipofectamine 3000 (Thermo Fisher Scientific, L3000001) according to the manufacturer's instructions.

4.14. Quantitative PCR Analysis. RNA was extracted from mouse kidneys using the TRIzol reagent. The RNA was reverse-transcribed using AMV Reverse Transcriptase (Promega) and a C1000 touch thermal cycler. SYBR green was used to quantify the real-time PCR products with a 7500 rpm real-time PCR system (Applied Biosystems). Thermocycler conditions were set up and operated based on the QC datasheet for the primers. The PCR primers used were specific to mice, including IL-10 (forward 5′ to 3′: GTCAGTCATTCTCGTCCGTCGTA; reverse 5′ to 3′: CGTCCTAAATTCCCAATGAACCC), SOD-1 (forward 5′ to 3′: CTCAGGAGAGCATTCCATCATT; reverse 5′ to 3′: CTCCCAG-CATTTCCAGTCTT), GAPDH (forward 5′ to 3′: TATGTCGTG-GAGTCTACTGGT; reverse 5′ to 3′: GAGTTGTCA-TATTTCTCGT), and ATP6a1 (forward 5′ to 3′: CTGTTATCCTCGGCATCATCCAC; reverse 5′ to 3′: CAGG-TAGCCAAACAACGAGGAC), and IL1β (forward 5′ to 3′: TCGCTCAGGGTCACAAGAAA; reverse 5′ to 3′: CATCAGAGG-CAAGGAGGAAAAC), and IL-18 (forward 5′ to 3′: ACTGTA-CAACCGCAGTAATACGG; reverse 5′ to 3′: GAGTGAACATTA-CAGATTTATCCC), p16 (forward 5′ to 3′: GAGGATACCCT-GATGGAGTATTTG; reverse 5′ to 3′: GCTATTAGGTCTGCCCTTTCTC), p21 (forward 5′ to 3′: GCAGACCAGCCTGACAGATTTC; reverse 5′ to 3′: TTCAGGGTTTTCTCTTGCAGAAG), and NQO-1 (forward 5′ to 3′: GCCGAACACAAGAAGCTGGAAG; reverse 5′ to 3′: GGCAAATCCTGCTACGAGCACT). The relative mRNA expression was determined using the comparative Ct method after normalizing to glyceraldehyde-3-phosphate dehydrogenase (GAPDH) expression.

4.15. Western Blot analysis. Cells and mouse kidney samples were harvested and suspended in lysis buffer [50 mM Tris−HCl (pH 7.5), 150 mM NaCl, 1 mM EDTA, 1% IGEPAL CA-630, 0.25% sodium deoxycholate, 0.1% sodium dodecyl sulfate (SDS), and protease inhibitors; Gendepot, P3100-001]. The cells were sonicated to disrupt them, and 20−40 μg of protein was subjected to SDS polyacrylamide gel electrophoresis, followed by transfer to nitro-cellulose membranes. After the mixture was blocked with 5% nonfat milk, primary and secondary antibodies were applied. Anti-COX4 (Abclonal A6564), anti-α-tubulin (Abclonal AC012), anti-GAPDH (Genetex GTX100118), anti-Drp1 (BD Biosciences 611112), NGAL (Santa Cruz sc-515876), and Pp65 (Santa Cruz sc-136548) antibodies were used. The protein bands were visualized using an ImageQuant Las 4000 mini (Amersham PLC, Amersham, U.K.) under optimal exposure conditions. ImageJ software (National Institutes of Health, Bethesda, MD) was used to measure the intensity of the bands.

4.16. CL Binding Assay. The intensity of NBD was measured to detect the interaction of NBD-labeled peptide or C6-NBD with liposomes.[56] For the association experiments, 1 μM NBD-labeled peptide in PBS was prepared in a black 96-well plate. Liposomes [POPC/POPE (2:1) or POPC/POPE (2:1) containing 10% CL] were added to the peptide to achieve the desired concentration. The mixture of NBD-peptide and liposomes was mixed through pipetting, and the fluorescence emission of the sample was monitored (λ_{ex} = 467 nm; λ_{em} = 536 nm).

For the association experiments influenced by CL proportion, 1 μM NBD-labeled peptide or C6-NBD in PBS was prepared in a black 96-well plate. Liposomes [POPC/POPE (2:1) containing 0−20% CL] were added to achieve a desired concentration of 5 μM, and the

solution was mixed through pipetting. The fluorescence emission of the sample was monitored (λ_{ex} = 467 nm; λ_{em} = 536 nm).

For the dissociation experiments, 1 μM NBD-labeled peptide in PBS was prepared in a black 96-well plate. Liposomes [POPC/POPE (2:1) or POPC/POPE (2:1) containing 10% CL] were added to the peptide to achieve a concentration of 100 μM. The mixture of NBD-peptide and liposomes was mixed through pipetting, and the fluorescence intensity of the mixture was measured (λ_{ex} = 467 nm; λ_{em} = 536 nm). Subsequently, an unlabeled peptide (acetylated peptide) was added to the mixture and mixed through pipetting. After a 10 min incubation in the dark, changes in fluorescence intensity were monitored. Peptide addition and fluorescence measurements were repeated, until the concentration of the acetylated peptide reached 40 μM.

4.17. Establishment of a CIN Model. Seven-week-old male C57BL/6 mice were purchased and subcutaneously injected with 20 mg/kg of colistin (Sigma-Aldrich, St. Louis, Missouri) each day for 7 days. Colistin-treated mice were peritoneally injected with 1 mg/kg CMP3013 once every other day. Briefly, 15 animals were randomly selected and divided into three groups (n = 5): CTL, colistin, and colistin + CMP3013. After 7 days, BUN was measured using an autoanalyzer (Wako Chemical Industries, Osaka, Japan). Creatinine was measured through the modified Jaffe reaction using an autoanalyzer (Hitachi Chemical Industries, Ltd., Osaka, Japan). The survival curves were analyzed when the CMP3013 peptide was administered to CIN mice. The Kaplan−Meier method and the survival rate were calculated and compared using log-rank (Mantel− Cox) test. Statistical analyses were conducted using GraphPad Prism. All animal experiments were performed with the approval of the Institutional Animal Care and Use Committee of the Clinical Research Institute at Seoul National University Hospital and in accordance with the Guidelines for the Care and Use of Laboratory Animals of the National Research Council (approval number: 210243S1A0).

4.18. Establishment of IRI Injury Model. A bilateral IRI model for AKI was established, and 1−5 mg/kg CMP3013 was injected intravenously (IV) 1 h prior to IRI. Briefly, a bilateral flank incision was made, and a microvascular clamp (Roboz Surgical Instrument, Gaithersburg, MD) was used to clamp both renal pedicles for 30 min. In sham-operated mice, both renal pedicles were exposed and ligated.[57]

4.19. Immunocytochemistry and Immunohistochemistry. Kidney sections were prepared, fixed in 10% formalin, and embedded in paraffin overnight. The 4 μm wide kidney sections were deparaffinized with xylene and dehydrated through graded alcohols. Antigen retrieval was achieved using 0.1 M sodium citrate and microwaving for 40 min. Subsequently, endogenous peroxidase in the samples was deactivated with 3% H_2O_2 in methanol for 15 min at room temperature. The sections were then washed with PBS and blocked with 10% normal goat serum, 5% bovine serum albumin, and 0.3% Triton X-100 in PBS for 1 h. The slides were stained with cytochrome C (Invitrogen, MA5-11674), 8-OHdG (Abcam, ab48508), P-21 (Santa Cruz, sc-6246), NGAL (Santa Cruz, sc-515876), F4/80 (Cell Signaling Technology, 70076S), and SOD-1 (Aviva Systems Biology, OABB00304) antibodies diluted with an antibody diluent (ZUC025, ZYTOMED, Berlin, Germany). Finally, the slides were washed with PBS and incubated for 1 h with EnVision$^+$ System HRP-Labeled Polymer conjugated antimouse or rabbit secondary antibody (K4001 or K4003, DKAO, Glostrup Municipality, Glostrup, Denmark). Mayer's hematoxylin (S3309, DAKO) was used for counterstaining the cell nuclei. Masson's trichrome staining (HT15, Sigma-Aldrich) was used to assess renal fibrosis and tubular necrosis. Histologic damage score calculation and image analysis were performed as described previously.[57] In addition, immunocytochemistry was performed as previously described,[58] with the exclusion of cytoplasmic extraction and the adoption of methanol fixation. For immunofluorescence, pp16 (Millipore Sigma, SAB4504720) and pp21 (Santa Cruz, sc-377569) primary antibodies were used. Stained slide images were captured by using a Leica inverted microscope (Leica Camera, Wetzlar, Germany). The LAS-4000 program (Leica) was used to quantify the positive areas (%).

4.20. Acute Hepatic Failure Mouse Model Induced by Thioacetamide (TAA) and Assessment of Liver Function. Seven-week-old female C57BL/6 mice were peritoneally injected with 1 mg/kg of CMP3013 three times a week before inducing acute liver failure by injecting 100 mg/kg of thioacetamide into the peritoneal cavity. After 6 days, serum samples were analyzed using a biochemical blood analyzer (Hitachi Chemical Industries, Ltd., Osaka, Japan). Aspartate aminotransferase and alanine aminotransferase were measured to evaluate the liver function. All animal experiments were approved by the Orientbio Animal Experimental Ethics Committee (approval number: ORIENT-IACUC-21158).

4.21. Statistical Analysis. All unpaired Student's t tests were performed using GraphPad Prism 9.0 software. Data are represented as means, and error bars denote standard deviations. Statistical significance was set at $p < 0.05$ and further defined according to the following p values: ns, $p > 0.05$; *, $p \leq 0.05$; **, $p \leq 0.01$; ***. $p \leq 0.001$; ****, $p \leq 0.0001$.

■ ASSOCIATED CONTENT

ⓈⒾ Supporting Information

The Supporting Information is available free of charge at https://pubs.acs.org/doi/10.1021/acs.jmedchem.3c01578.

> Chromatograms of the dimer bundle peptides (Figure S1); comparison of cell permeability among peptides (Figure S2); comparison of air-oxidized CMP3013 and antiparallel CMP3013 (Figure S3); verification of subcellular fractionation (Figure S4); inhibition of cellular ROS generation by CMP3013 (Figure S5); mitochondria targeting by diLR10 and effects on intracellular ROS levels (Figure S6); localization of CMP3013 with fissioned mitochondria (Figure S7); prevention of CCCP-induced cell death by CMP3013 (Figure S8); beneficial effects of CMP3013 to human cells against mitochondria-damaging conditions (Figure S9); sequences, mass spectrometry data, and chromatograms of NBD-CMP3013 monomer and NBD-SS-31 (Figure S10); cell penetration, cellular localization, and enhancement of ATP synthesis by CMP3013 in hTECs (Figure S11); effects of CMP3013 on colistin-damaged kidneys in a mouse CIN model (Figure S12); antiapoptotic role and the regulation of cyclin-dependent kinase activity of CMP3013 in hTECs (Figure S13); effects of CMP3013 on acute kidney injury in a mouse ischemia-reperfusion injury (IRI) model (Figure S14); therapeutic effectiveness of CMP3013 in acute liver injury mouse models (Figure S15); sequences and mass spectrometry data of the monomer peptides (Table S1); sequences and mass spectrometry data of the dimer bundle peptides (Table S2); and sequences and mass spectrometry data of the TAMRA-labeled dimer bundle peptides (Table S3) (PDF)
>
> Molecular formula strings (CSV)
>
> Supplementary movie file 1 (MP4)

■ AUTHOR INFORMATION

Corresponding Authors

Yon Su Kim − *Department of Internal Medicine, Seoul National University Hospital, Seoul 03080, Korea; Kidney Research Institute, Seoul National University, Seoul 03080, Korea; Biomedical Research Institute, Seoul National University Hospital, Seoul 03080, Republic of Korea;* Email: yonsukim@snu.ac.kr

Seung Hee Yang − *Kidney Research Institute, Seoul National University, Seoul 03080, Korea; Biomedical Research Institute, Seoul National University Hospital, Seoul 03080, Republic of Korea*; Email: ysh5794@gmail.com

Jaehoon Yu − *Department of Chemistry & Education, Seoul National University, Seoul 08826, Korea; CAMP Therapeutics Co., Ltd., Seoul 08826, Korea;* ● orcid.org/0000-0003-4222-4398; Email: jhoonyu@snu.ac.kr

Authors

Gwangsu Shin − *Department of Chemistry & Education, Seoul National University, Seoul 08826, Korea*

Soonsil Hyun − *Department of Chemistry & Education, Seoul National University, Seoul 08826, Korea;* ● orcid.org/0000-0002-3400-7353

Dongwoo Kim − *Department of Chemistry & Education, Seoul National University, Seoul 08826, Korea*

Yoonhwa Choi − *CAMP Therapeutics Co., Ltd., Seoul 08826, Korea*

Kyu Hong Kim − *Department of Biomedical Sciences, Seoul National University Graduate School, Seoul 03080, Korea*

Dongmin Kim − *CAMP Therapeutics Co., Ltd., Seoul 08826, Korea*

Soie Kwon − *Department of Internal Medicine, Seoul National University Hospital, Seoul 03080, Korea*

Complete contact information is available at:
https://pubs.acs.org/10.1021/acs.jmedchem.3c01578

Author Contributions

G.S. led the data curation, analysis, validation, and writing of the manuscript. S.H., Dongwoo K., Y.C., K.H.K., Dongmin K., and S.K. contributed to data curation, analysis, and validation. Y.S.K. and S.H.Y. contributed to the design of the investigation, project administration, and manuscript preparation. J.Y. contributed to funding acquisition, investigation, project administration, and manuscript preparation.

Notes

The authors declare the following competing financial interest(s): JY, Dongmin K, and YC are employees of CAMP Therapeutics. This manuscript is based on a company-owned patent.

■ ABBREVIATIONS USED

CL, cardiolipin; IMM, inner mitochondrial membrane; ROS, reactive oxygen species; AKI, acute kidney injury; CIN, colistin-induced nephrotoxicity; EC_{50}, effective concentration 50; CCCP, carbonyl cyanide *m*-chlorophenylhydrazone; DLCL, dilysoCL; NAO, nonyl acridine orange; hTECs, human tubular epithelial cells; NGAL, neutrophil gelatinase-associated lipocalin

■ REFERENCES

(1) Wallace, D. C. Mitochondrial Genetic Medicine. *Nat. Genet.* **2018**, *50*, 1642−1649.

(2) Tönnies, E.; Trushina, E. Oxidative Stress, Synaptic Dysfunction, and Alzheimer's Disease. *J. Alzheimers Dis.* **2017**, *57*, 1105−1121.

(3) Li, X.; Zhang, W.; Cao, Q.; Wang, Z.; Zhao, M.; Xu, L.; Zhuang, Q. Mitochondrial Dysfunction in Fibrotic Diseases. *Cell Death Discovery* **2020**, *6*, No. 80.

(4) Ikon, N.; Ryan, R. O. Cardiolipin and Mitochondrial Cristae Organization. *Biochim. Biophys. Acta, Biomembr.* **2017**, *1859*, 1156−1163.

(5) Falabella, M.; Vernon, H. J.; Hanna, M. G.; Claypool, S. M.; Pitceathly, R. D. S. Cardiolipin, Mitochondria, and Neurological Disease. *Trends Endocrinol. Metab.* **2021**, *32*, 224−237.

(6) Liu, N. K.; Deng, L. X.; Wang, M.; Lu, Q. B.; Wang, C.; Wu, X.; Wu, W.; Wang, Y.; Qu, W.; Han, Q.; Xia, Y.; Ravenscraft, B.; Li, J. L.; You, S. W.; Wipf, P.; Han, X.; Xu, X. M. Restoring Mitochondrial Cardiolipin Homeostasis Reduces Cell Death and Promotes Recovery After Spinal Cord Injury. *Cell Death Discovery* **2022**, *13*, No. 1058.

(7) Strazdauskas, A.; Trumbeckaite, S.; Jakstas, V.; Kamarauskaite, J.; Ivanauskas, L.; Baniene, R. Ischemia In Vivo Induces Cardiolipin Oxidation in Rat Kidney Mitochondria. *Biology* **2022**, *11*, 541.

(8) Paradies, G.; Paradies, V.; Ruggiero, F. M.; Petrosillo, G. Role of Cardiolipin in Mitochondrial Function and Dynamics in Health and Disease: Molecular and Pharmacological Aspects. *Cells* **2019**, *8*, 728.

(9) He, B.; Yu, H.; Liu, S.; Wan, H.; Fu, S.; Liu, S.; Yang, J.; Zhang, Z.; Huang, H.; Li, Q.; Wang, F.; Jiang, Z.; Liu, Q.; Jiang, H. Mitochondrial Cristae Architecture Protects Against mtDNA Release and Inflammation. *Cell Rep.* **2022**, *41*, No. 111774.

(10) Zhao, K.; Luo, G.; Giannelli, S.; Szeto, H. H. Mitochondria-Targeted Peptide Prevents Mitochondrial Depolarization and Apoptosis Induced by Tert-Butyl Hydroperoxide in Neuronal Cell Lines. *Biochem. Pharmacol.* **2005**, *70*, 1796−1806.

(11) Mitchell, W.; Ng, E. A.; Tamucci, J. D.; Boyd, K.; Sathappa, M.; Coscia, A.; Pan, M.; Han, X.; Eddy, N. A.; May, E. R.; et al. Molecular Mechanism of Action of Mitochondrial Therapeutic SS-31 (Elamipretide): Membrane Interactions and Effects on Surface Electrostatics. *bioRxiv* **2019**, No. 735001.

(12) Chamberlain, G. R.; Tulumello, D. V.; Kelley, S. O. Targeted Delivery of Doxorubicin to Mitochondria. *ACS Chem. Biol.* **2013**, *8* (8), 1389−1395.

(13) Jang, S.; Hyun, S.; Kim, S.; Lee, S.; Lee, I. S.; Baba, M.; Lee, Y.; Yu, J. Cell-Penetrating, Dimeric *α*-Helical Peptides: Nanomolar Inhibitors of HIV-1 Transcription. *Angew. Chem.* **2014**, *126*, 10250−10253.

(14) Hyun, S.; Kim, D.; Cho, J.; Jeong, D.; Chung, D. H.; Yu, J. Design and Optimization of an *α*-Helical Bundle Dimer Cell-Penetrating Peptide for In Vivo Drug Delivery. *Bioconjugate Chem.* **2022**, *33* (12), 2420−2427, DOI: 10.1021/acs.bioconjchem.2c00518.

(15) Horton, K. L.; Stewart, K. M.; Fonseca, S. B.; Guo, Q.; Kelley, S. O. Mitochondria-Penetrating Peptides. *Chem. Biol.* **2008**, *15*, 375−382.

(16) Dong, Y.; Zhang, Q.; Wen, J.; Chen, T.; He, L.; Wang, Y.; Yin, J.; Wu, R.; Xue, R.; Li, S.; Fan, Y.; Wang, N. Ischemic Duration and Frequency Determines AKI-to-CKD Progression Monitored by Dynamic Changes of Tubular Biomarkers in IRI Mice. *Front. Physiol.* **2019**, *10*, 153.

(17) Han, S. J.; Lee, H. T. Mechanisms and Therapeutic Targets of Ischemic Acute Kidney Injury. *Kidney Res. Clin. Pract.* **2019**, *38*, 427−440.

(18) Packialakshmi, B.; Stewart, I. J.; Burmeister, D. M.; Chung, K. K.; Zhou, X. Large Animal Models for Translational Research in Acute Kidney Injury. *Renal Failure* **2020**, *42*, 1042−1058.

(19) Feng, J. Y.; Lee, Y. T.; Pan, S. W.; Yang, K. Y.; Chen, Y. M.; Yen, D. H.-T.; Li, S. Y.; Wang, F. D. Comparison of Colistin-Induced Nephrotoxicity Between Two Different Formulations of Colistin in Critically Ill Patients: A Retrospective Cohort Study. *Antimicrob. Resist. Infect. Control* **2021**, *10*, No. 111.

(20) Malik, S. S.; Mundra, S. Increasing Consumption of Antibiotics During the COVID-19 Pandemic: Implications for Patient Health and Emerging Anti-Microbial Resistance. *Antibiotics* **2023**, *12*, 45.

(21) Gai, Z.; Samodelov, S. L.; Kullak-Ublick, G. A.; Visentin, M. Molecular Mechanisms of Colistin-Induced Nephrotoxicity. *Molecules* **2019**, *24*, 653.

(22) Bhatia, D.; Capili, A.; Choi, M. E. Mitochondrial Dysfunction in Kidney Injury, Inflammation, and Disease: Potential Therapeutic Approaches. *Kidney Res. Clin. Pract.* **2020**, *39*, 244−258.

(23) Mitchell, W.; Tamucci, J. D.; Ng, E. L.; Liu, S.; Szeto, H. H.; May, E. R.; Alexandrescu, A. T.; Alder, N. N. Structure-Activity Relationships in the Design of Mitochondria-Targeted Peptide Therapeutics. *bioRxiv* **2021**, DOI: 10.1101/2021.11.08.467832.

(24) Mitchell, W.; Ng, E. A.; Tamucci, J. D.; Boyd, K. J.; Sathappa, M.; Coscia, A.; Pan, M.; Han, X.; Eddy, N. A.; May, E. R.; Szeto, H. H.; Alder, N. N. The Mitochondria-Targeted Peptide SS-31 Binds Lipid Bilayers and Modulates Surface Electrostatics as a Key Component of Its Mechanism of Action. *J. Biol. Chem.* **2020**, *295*, 7452−7469.

(25) Hyun, S.; Lee, Y.; Jin, S. M.; Cho, J.; Park, J.; Hyeon, C.; Kim, K. S.; Lee, Y.; Yu, J. Oligomer Formation Propensities of Dimeric Bundle Peptides Correlate with Cell Penetration Abilities. *ACS Cent. Sci.* **2018**, *4*, 885−893.

(26) Liu, X.; Hajnóczky, G. Altered Fusion Dynamics Underlie Unique Morphological Changes in Mitochondria During Hypoxia-Reoxygenation Stress. *Cell Death Differ.* **2011**, *18*, 1561−1572.

(27) Ahmad, T.; Aggarwal, K.; Pattnaik, B.; Mukherjee, S.; Sethi, T.; Tiwari, B. K.; Kumar, M.; Micheal, A.; Mabalirajan, U.; Ghosh, B.; Sinha Roy, S.; Agrawal, A. Computational Classification of Mitochondrial Shapes Reflects Stress and Redox State. *Cell Death Discovery* **2013**, *4*, No. e461.

(28) Tong, M.; Zablocki, D.; Sadoshima, J. The Role of Drp1 in Mitophagy and Cell Death in the Heart. *J. Mol. Cell. Cardiol.* **2020**, *142*, 138−145.

(29) Miyazono, Y.; Hirashima, S.; Ishihara, N.; Kusukawa, J.; Nakamura, K. I.; Ohta, K. Uncoupled Mitochondria Quickly Shorten Along Their Long Axis to Form Indented Spheroids, Instead of Rings, in a Fission-Independent Manner. *Sci. Rep.* **2018**, *8*, No. 350.

(30) Koncha, R. R.; Ramachandran, G.; Sepuri, N. B. V.; Ramaiah, K. V. A. CCCP-Induced Mitochondrial Dysfunction - Characterization and Analysis of Integrated Stress Response to Cellular Signaling and Homeostasis. *FEBS J.* **2021**, *288*, 5737−5754.

(31) Wollweber, F.; von der Malsburg, K.; van der Laan, M. Mitochondrial Contact Site and Cristae Organizing System: A Central Player in Membrane Shaping and Crosstalk. *Biochim. Biophys. Acta, Mol. Cell Res.* **2017**, *1864*, 1481−1489.

(32) Dudek, J. Role of Cardiolipin in Mitochondrial Signaling Pathways. *Front. Cell Dev. Biol.* **2017**, *5*, 90.

(33) Ding, W. X.; Ni, H. M.; Li, M.; Liao, Y.; Chen, X.; Stolz, D. B.; Dorn, G. W.; Yin, X. M. Nix Is Critical to Two Distinct Phases of Mitophagy, Reactive Oxygen Species-Mediated Autophagy Induction and Parkin-Ubiquitin-p62-Mediated Mitochondrial Priming. *J. Biol. Chem.* **2010**, *285*, 27879−27890.

(34) Cen, X.; Chen, Y.; Xu, X.; Wu, R.; He, F.; Zhao, Q.; Sun, Q.; Yi, C.; Wu, J.; Najafov, A.; Xia, H. Pharmacological Targeting of MCL-1 Promotes Mitophagy and Improves Disease Pathologies in an Alzheimer's Disease Mouse Model. *Nat. Commun.* **2020**, *11*, No. 5731.

(35) Goldstein, A.; Barrett, R. W. Ligand Dissociation Constants from Competition Binding Assays: Errors Associated with Ligand Depletion. *Mol. Pharmacol.* **1987**, *31*, 603−609.

(36) Raghuraman, H.; Chattopadhyay, A. Orientation and Dynamics of Melittin in Membranes of Varying Composition Utilizing NBD Fluorescence. *Biophys. J.* **2007**, *92*, 1271−1283.

(37) Yousef, J. M.; Chen, G.; Hill, P. A.; Nation, R. L.; Li, J. Ascorbic Acid Protects Against the Nephrotoxicity and Apoptosis Caused by Colistin and Affects Its Pharmacokinetics. *J. Antimicrob. Chemother.* **2012**, *67*, 452−459.

(38) Dai, C.; Tang, S.; Wang, Y.; Velkov, T.; Xiao, X. Baicalein Acts as a Nephroprotectant That Ameliorat*es Coli*stin-Induced Nephrotoxicity by Activating the Antioxidant Defence Mechanism of the Kidneys and Down-Regulating the Inflammatory Response. *J. Antimicrob. Chemother.* **2017**, *72*, 2562−2569.

(39) Ross, D.; Siegel, D. Functions of NQO1 in Cellular Protection and CoQ10 Metabolism and Its Potential Role as a Redox Sensitive Molecular Switch. *Front. Physiol.* **2017**, *8*, 595.

(40) Hong, Y. A.; Park, C. W. Catalytic Antioxidants in the Kidney. *Antioxidants* **2021**, *10*, 130.

(41) Haddad, J. J.; Fahlman, C. S. Redox- and Oxidant-Mediated Regulation of Interleukin-10: An Anti-Inflammatory, Antioxidant Cytokine? *Biochem. Biophys. Res. Commun.* **2002**, *297*, 163−176.

(42) Moreno-Loshuertos, R.; Movilla, N.; Marco-Brualla, J.; Soler-Agesta, R.; Ferreira, P.; Enríquez, J. A.; Fernández-Silva, P. A Mutation in Mouse MT-ATP6 Gene Induces Respiration Defects and Opposed Effects on the Cell Tumorigenic Phenotype. *Int. J. Mol. Sci.* **2023**, *24*, 1300.

(43) He, Q.; Harris, N.; Ren, J.; Han, X. Mitochondria-Targeted Antioxidant Prevents Cardiac Dysfunction Induced by Tafazzin Gene Knockdown in Cardiac Myocytes. *Oxid. Med. Cell. Longevity* **2014**, *2014*, No. 654198.

(44) Ding, Y.; Jiang, Z.; Xia, B.; Zhang, L.; Zhang, C.; Leng, J. Mitochondria-Targeted Antioxidant Therapy for an Animal Model of PCOS-IR. *Int. J. Mol. Med.* **2019**, *43*, 316−324.

(45) Paradies, G.; Petrosillo, G.; Paradies, V.; Reiter, R. J.; Ruggiero, F. M. Melatonin, Cardiolipin and Mitochondrial Bioenergetics in Health and Disease. *J. Pineal Res.* **2010**, *48*, 297−310.

(46) Li, J.; Romestaing, C.; Han, X.; Li, Y.; Hao, X.; Wu, Y.; Sun, C.; Liu, X.; Jefferson, L. S.; Xiong, J.; Lanoue, K. F.; Chang, Z.; Lynch, C. J.; Wang, H.; Shi, Y. Cardiolipin Remodeling by ALCAT1 Links Oxidative Stress and Mitochondrial Dysfunction to Obesity. *Cell Metab.* **2010**, *12*, 154−165.

(47) Liu, X.; Zhang, J.; Li, J.; Song, C.; Shi, Y. Pharmacological Inhibition of ALCAT1 Mitigates Amyotrophic Lateral Sclerosis by Attenuating SOD1 Protein Aggregation. *Mol. Metab.* **2022**, *63*, No. 101536.

(48) Lightowlers, R. N.; Chrzanowska-Lightowlers, Z. M.; Russell, O. M. Mitochondrial Transplantation-a Possible Therapeutic for Mitochondrial Dysfunction?: Mitochondrial Transfer Is a Potential Cure for Many Diseases but Proof of Efficacy and Safety Is Still Lacking. *EMBO Rep.* **2020**, *21* (9), No. e50964.

(49) Kellum, J. A.; Romagnani, P.; Ashuntantang, G.; Ronco, C.; Zarbock, A.; Anders, H. J. Acute Kidney Injury. *Nat. Rev. Dis. Primers* **2021**, *7*, No. 52.

(50) Perez Ruiz de Garibay, A.; Kortgen, A.; Leonhardt, J.; Zipprich, A.; Bauer, M. Critical Care Hepatology: Definitions, Incidence, Prognosis and Role of Liver Failure in Critically Ill Patients. *Crit. Care* **2022**, *26*, No. 289.

(51) Andreev, K.; Bianchi, C.; Laursen, J. S.; Citterio, L.; Hein-Kristensen, L.; Gram, L.; Kuzmenko, I.; Olsen, C. A.; Gidalevitz, D. Guanidino Groups Greatly Enhance the Action of Antimicrobial Peptidomimetics Against Bacterial Cytoplasmic Membranes. *Biochim. Biophys. Acta, Biomembr.* **2014**, *1838*, 2492−2502.

(52) Lee, J.; Lee, Y.; Kim, K. H.; Kim, D. K.; Joo, K. W.; Shin, S. J.; Kim, Y. S.; Yang, S. H. Chemokine (C-C Motif) Ligand 8 and Tubulo-Interstitial Injury in Chronic Kidney Disease. *Cells* **2022**, *11*, 658.

(53) Wieckowski, M. R.; Giorgi, C.; Lebiedzinska, M.; Duszynski, J.; Pinton, P. Isolation of Mitochondria-Associated Membranes and Mitochondria from Animal Tissues and Cells. *Nat. Protoc.* **2009**, *4*, 1582−1590.

(54) Wang, Y.; Lu, M.; Xiong, L.; Fan, J.; Zhou, Y.; Li, H.; Peng, X.; Zhong, Z.; Wang, Y.; Huang, F.; Chen, W.; Yu, X.; Mao, H. Drp1-Mediated Mitochondrial Fission Promotes Renal Fibroblast Activation and Fibrogenesis. *Cell Death Discovery* **2020**, *11*, No. 29.

(55) Youk, J.; Kim, T.; Evans, K. V.; Jeong, Y. I.; Hur, Y.; Hong, S. P.; Kim, J. H.; Yi, K.; Kim, S. Y.; Na, K. J.; Bleazard, T.; Kim, H. M.; Fellows, M.; Mahbubani, K. T.; Saeb-Parsy, K.; Kim, S. Y.; Kim, Y. T.; Koh, G. Y.; Choi, B. S.; Ju, Y. S.; Lee, J. H. Three-Dimensional Human Alveolar Stem Cell Culture Models Reveal Infection Response to SARS-CoV-2. *Cell Stem Cell* **2020**, *27*, 905−919.

(56) Merklinger, E.; Gofman, Y.; Kedrov, A.; Driessen, A. J.; Ben-Tal, N.; Shai, Y.; Rapaport, D. Membrane Integration of a

Mitochondrial Signal-Anchored Protein Does Not Require Additional Proteinaceous Factors. *Biochem. J.* **2012**, *442*, 381−389.

(57) Park, J. Y.; Yoo, K. D.; Bae, E.; Kim, K. H.; Lee, J. W.; Shin, S. J.; Lee, J. S.; Kim, Y. S.; Yang, S. H. Blockade of STAT3 Signaling Alleviates the Progression of Acute Kidney Injury to Chronic Kidney Disease Through Antiapoptosis. *Am. J. Physiol. Renal Physiol.* **2022**, *322*, F553−F572.

(58) Shin, G.; Jeong, D.; Kim, H.; Im, J. S.; Lee, J. K. RecQL4 Tethering on the Pre-replicative Complex Induces Unscheduled Origin Activation and Replication Stress in Human Cells. *J. Biol. Chem.* **2019**, *294*, 16255−16265.